Development of a Two-dimensional, Moving Mesh Treatment for Modelling the Reaction Chamber of the Soluble Lead Flow Battery as a Function of State of Charge for Pb and PbO_2 Deposition and Dissolution

E.J. Fraser[1], K.K.J. Ranga Dinesh[1] and R.G.A. Wills[1*]

1. Energy Technology Research Group, Faculty of Engineering and Physical Sciences, University of Southampton, SO17 1BJ (UK).

Abstract:

During cycling of the soluble lead flow battery, solid layers of lead (Pb) and lead dioxide (PbO_2) are deposited and stripped from the electrode surfaces. As such, there is a change in geometry of the flow field within the battery. A detailed two-dimensional numerical model which simulates this change in geometry using a moving mesh technique is developed. The model accounts for deposition of Pb, PbO_2 along with the formation of lead oxide (PbO) during discharge of the PbO_2 deposit due to a side reaction which is commonly assumed in the literature. Over short time scales of around 1 hr charge/discharge periods, which are typically reported in the literature, the effect of this is small. However, over more realistic time scales (>1 hr), by applying this technique, significant differences are seen in the cell resistance and in the mass flow rate of electrolyte. As a result, a difference in cell voltage of up to 65 mV is seen over a 24 hour period. The numerical results are validated against experimental data, showing an agreement in the voltage-time profile and a close fit for the moving mesh approach.

Keywords: Energy storage, Soluble lead flow battery, Modelling & simulation, Moving mesh, Cell resistance.

Highlights

- Impact of changing electrode geometries on the soluble lead flow battery performance.

- Performed unsteady two-dimensional numerical calculation.

- Decrease in cell resistance over long time periods when moving mesh is used.

- Demonstration literature static mesh assumptions are not valid at high capacity.

[*] **Corresponding Author**:

Richard Wills, University of Southampton, Faculty of Engineering and Physical Sciences, Highfield, Southampton, SO17 1BJ (UK). rgaw@soton.ac.uk

1 Introduction

An increasing penetration of renewable energy generation in electricity networks is creating a case for widespread, large scale energy storage. A number of energy storage technologies have been proposed [1]. Redox flow batteries (RFBs) are one such set of technologies, which are suited to large scale energy storage (>MW, MWh). There is substantial literature describing a large number of proposed chemistries for RFBs [2-7]. These systems cover a range of technology readiness levels, including several demonstrator and commercial systems; the vast majority of which use the all-vanadium chemistry [8]. Another promising chemistry is the soluble lead flow battery (SLFB). The SLFB has a number of benefits over other RFBs. Unlike conventional RFBs, both the positive and the negative reaction in the SLFB use the same ion, Pb^{2+}, and hence it can operate with just a single electrolyte in an undivided configuration. There is also an existing supply chain for production and recycling of lead so problems with supply and disposal, such as those seen with lithium ion batteries, are reduced.

The SLFB is based on a soluble lead species, Pb^{2+}, dissolved in methanesulfonic acid (MSA), an acid that is widely regarded as being less environmentally damaging than many other acids [9]. During charge, Pb^{2+} is reduced to solid Pb and oxidised to solid PbO_2 and plated onto the negative and positive electrodes, respectively. Dissolution of the solid deposits back to Pb^{2+} in solution occurs during discharge. The reactions involved in the battery are:

$$Positive \qquad Pb^{2+} + 2H_2O \rightleftharpoons PbO_2 + 4H^+ + 2e^- \qquad E^0 = +1.46\ V\ vs\ SHE$$

$$Negative \qquad Pb^{2+} + 2e^- \rightleftharpoons Pb \qquad E^0 = -0.13\ V\ vs\ SHE$$

$$Cell \qquad 2Pb^{2+} + 2H_2O \rightleftharpoons Pb + PbO_2 + 4H^+ \qquad E^0_{cell} = +1.59\ V$$

Where left to right is charging the battery. The electrode potentials are given vs the standard hydrogen electrode (SHE).

As Pb and PbO_2 are deposited onto the electrodes, there is clearly a change in geometry. At higher states of charge, there are larger deposits and consequently a smaller effective inter-electrode gap.

This smaller gap will affect the pressure drop through the cell. The resistance of the cell will also change, as there is a shorter diffusion path for conduction through the electrolyte but an increased resistance through the solid phase as deposit thickness increases. The desired capacity of the SLFB will, in part, dictate the inter-electrode gap of the system.

Scale-up of the SLFB is required for commercial operation. While scale-up of flow batteries is less problematic than with conventional batteries, issues still exist when operating the SLFB over long timescales and at a large scale. Numerical modelling and simulation can be used to identify local characteristics more explicitly, such as local flow behaviour and concentration of the electrolyte. It can be used to provide design guidelines for further optimisation of the SLFB.

To gain full advantage from an energy storage technology, it is favourable to be able to stack the services it can provide, allowing for multiple revenue streams [10]. Typical flow battery services such as load levelling may require up to 10 hours of storage capacity. Furthermore, services such as back-up of renewable generation may require several days of storage [11]. To be competitive in several markets, it is therefore important that the soluble lead flow battery is capable of long term energy storage.

Several authors have numerically modelled the SLFB. Shah et al. [12], Bates et al. [13], Oury et al. [14], and Nandanwar and Kumar [15-17], have performed two dimensional, numerical simulations that consider the flow conditions as well as the kinetics of electrode reactions and the mass transport of Pb^{2+}, H^+ and a negative counter ion in an aqueous electrolyte. With the exception of Oury et al. [14], who simulated the steady state of the system, all previous SLFB models have simulated the transient behaviour of the battery. Nandanwar and Kumar, [15-17], and Oury et al., [14], used the methanesulfonate ion, $CH_3SO_3^-$ as a counter ion. Shah et al., [12] also employed the methanesulfonate ion; however, in their methodology, the sulphuric acid anion, HSO_4^- is used. Bates et al., [13], also used HSO_4^- as the counterion. Pb^{2+} is insoluble in sulphuric acid and sulphuric acid is likely to dissociate further to SO_4^{2-} so it is unclear why this is used rather than $CH_3SO_3^-$.

Shah et al. produced the first SLFB model [12]. Their work focused on the effect of different current densities on the performance of the SLFB and shows that, as seen in experimental results, the coulombic efficiency (defined as the total charge drawn from the cell during discharge divided by the total charge applied to the cell during charge) of the system decreases as current density increases. They successfully simulated the two-step charging mechanism of the SLFB by including oxidation of the solid oxide deposit at the positive electrode. Bates et al. [13] have produced a model of the SLFB and have run simulations to show the effect of different operating conditions on the performance of the SLFB. An increase in temperature is shown to increase the overpotential. However, the authors use several unrealistic conditions in the study, including simulations of the SLFB at 600 K – a temperature which is significantly higher than the boiling point of the electrolyte and close to the melting point of lead. Oury et al. [14] proposed a novel honeycomb positive electrode design. Their proposed design provides an increase in surface area of the positive electrode compared with the negative electrode in an attempt to reduce the overpotentials associated with the positive reaction. This design consists of a positive flow through electrode sandwiched between two planar negative electrodes and hence a stack of cells manufactured in such a way could not be arranged to form a bipolar stack. Significant further work would also be required to provide even flow of electrolyte over the electrodes. Nandanwar and Kumar first investigated non-uniform current densities [17]. Then they studied the voltage spike/trough at the start of charges/discharges, which they termed the coup de fouet effect [15]. Most recently, they have incorporated free convection into their model. Free convection is the movement of the electrolyte due to its change in density. The authors compared two cases, forced convection, i.e. the flow is only due to pumping and mixed convection where both free and forced convection are considered. They concluded that at higher current densities (> 30 mA cm^{-2}) free convection becomes dominant and the system is able to run with a negligible applied flow rate [16].

Shah et al. [12], Nandanwar and Kumar [15-17], and Bates et al. [13] have all considered a side reaction involving PbO which leads to the characteristic two-step voltage profile during the second and all subsequent charges. Oury et al. [14] did not include side reactions and only simulated a cell at steady state, assuming constant concentration at the inlet.

All previous numerical models included a degree of experimental validation. For example, Shah et al. [12] validated numerical data over three different current densities, 10, 20 and 30 mA cm^{-2}. Their model provides a close match in all cases. Nandanwar and Kumar [17] validated their model over two full charge-discharge cycles and obtained good agreement with the experimental data. Bates et al. validated their numerical results over the first two charges and the first discharge at 15 mA cm^{-2} and found reasonable agreement with the experimental data [13]. However, the two-step charging mechanism is more pronounced in simulated results than is seen in their experimental validation.

Oury et al. have validated numerical results with the experimental data over the first six cycles [14]. However, they did not consider any side reactions in their calculation, so the voltage response is not applicable to a large proportion of the second and subsequent charges. Nevertheless, good agreement was found during discharge and for the later part of second and subsequent discharge cycles. A change in concentration due to incomplete discharges causes the voltage to progressively increase with cycle number. The model captures this.

In all previous SLFB models, Navier-Stokes equations were employed to simulate the flow of electrolyte. There are two approaches used in the literature to model the flow of electrolyte through the battery: the fluid equations can be solved at steady state before solving the rest of the model, or they can be solved transiently concurrently with the rest of the model. For example, Nandanwar and Kumar [15-17] and Bates et al., [13] performed steady-state simulations as constant fluid properties were assumed. Shah et al. carried out unsteady variable density simulations as the density of the electrolyte was not kept constant [12]. All studies assumed an incompressible fluid and as such, keep the viscosity constant.

Furthermore, Bates et al. considered the effects of temperature on the performance of the SLFB in their model [13]. However, the model was run at 300 K, 350 K, 400 K and 600 K. Which, as previously mentioned, at an assumed outlet pressure of 3 bar, at the highest two temperatures the electrolyte would boil.

Typically flow batteries operate at current densities ranging between 20 and 100 mA cm^{-2}[3, 5, 18] and a report on the SLFB has suggested a target of 50 mA cm^{-2} or higher for commercial operation [19]. As additional capacity is generally lower cost than additional power in RFBs, a higher ratio of energy to power will make them more competitive. In the SLFB, at these current densities, a large capacity to power ratio would lead to thicker deposits than the maximum thickness suggested by Pletcher et al., [20], for efficient operation with a long cycle life. The effect of these thick deposits must be understood for optimal cell performance. A comprehensive review of the SLFB by Krishna et al. also highlighted the lack of understanding of the effect of the change in geometry of the deposits during operation [2].

This study proposes a numerical model that simulates the change in thickness of the deposits at the electrodes of the SLFB. A novel technique using a moving mesh is applied to model this change in geometry during operation. To the best of our knowledge, the methodology described in this paper represents the first numerical modelling work of the soluble lead flow battery, using a moving mesh technique to accurately predict the change in thickness of the deposits at the electrodes. The remaining sections present how this technique is implemented and what the effects of this change in geometry have on the performance of the SLFB.

2 Experimental

Experimental validation was carried out using a cell that was previously designed and made by Southampton and CTech Innovation ltd as part of the Department of Energy and Climate Change (DECC) Energy Storage Component Research & Feasibility Study Scheme – A soluble lead redox flow battery demonstrator (PBatt). It consisted of a PEEK flow frame, used to distribute the flow over the electrodes and hold the electrodes in place with an inter-electrode gap of 1.2 cm. The cell was compressed by two stainless steel end plates fixed with 12 bolts. Both electrodes were Entegris carbon polymer plates. Brass plate current collectors were employed and the cell was sealed using

Viton gaskets. The exposed area of each electrode was 10 cm × 10 cm. 1000 cm^3 of electrolyte was circulated through the system using a Cole-Parmer Masterflex peristaltic pump, set to a constant speed so that the mean velocity over the electrode surfaces was 2.3 cm s^{-1} when no deposit was present. The electrolyte consisted of an aqueous solution of 0.5 mol dm^{-3} methanesulfonic acid (CH_3SO_3H) and 0.7 mol dm^{-3} lead methanesulfonate ($Pb(CH_3SO_3)_2$). An MTI 8-channel battery analyser was used to measure the cell potential and supply and draw constant currents during charge and discharge.

3 Model Methodology

A detailed, two dimensional, transient numerical model is employed to simulate the operation of the soluble lead flow battery including conservation of mass and momentum of the electrolyte and the Nernst Planck equation to simulate mass transport of the dissolved species. The model is divided into solid domains for the positive and negative electrodes and a fluid domain where the electrolyte flows between the electrodes. The remaining parts of the system, including the reservoir and flow circuitry, are not explicitly modelled.

The model uses the reactions highlighted in the previous section. Several side reactions are known to occur in the SLFB, including oxygen and hydrogen evolution. The exact mechanism for the positive half-reaction is not well understood. However, following the lead of previous models in the literature [12], a single side reaction is assumed for the positive electrode:

Positive side reaction $$PbO + H_2O \leftrightarrow PbO_2 + 2H^+ + 2e^- \qquad E^0 = +0.28\,V\ vs\ SHE$$

As this reaction involves PbO_2, which is formed during discharge, it is only present after the first charge and leads to the characteristic two-step charging mechanism of the SLFB. This is illustrated in cell voltage profile of the second and all subsequent charge steps by the potential starting at a lower voltage before rising to the potential of the first charge later in the step [21].

3.1 Assumptions

It is assumed that perfect mixing occurs in the reservoir. In other words, the electrolyte composition is homogeneous at the cell inlet and accounts for both the outlet concentration and the reservoir concentration. The electrolyte is composed of dissociated H^+, Pb^{2+} and $CH_3SO_3^-$ ions in H_2O. The electroneutrality condition is implemented to maintain charge balance within the electrolyte. Using a maximum electrolyte density of 1.2 g cm^{-3}, a minimum viscosity of 1.0 mPa, a characteristic length of 2.0 cm and a fluid velocity of 2.3 cm s^{-1}, the Reynolds number for the system is calculated to be ~550. For flow between parallel plates with Re << 2300 laminar flow can be assumed [22]. High-quality, fully dense, smooth, even deposits are assumed to form at both electrodes. There is no gas evolution at the electrodes. It is also assumed that the average velocity of the electrolyte is constant.

3.2 Governing equations

The fluid flow is described using the laminar form of Navier-Stokes and Continuity equations.

$$\rho\frac{\partial \boldsymbol{u}}{\partial t} + \rho(\boldsymbol{u}\cdot\nabla)\boldsymbol{u} = \nabla\cdot[-p + \mu\nabla\boldsymbol{u}] \qquad (2.1)$$

$$\nabla\cdot\boldsymbol{u} = 0 \quad (2.2)$$

Where **u** is the liquid velocity in m s^{-1}, p is the pressure in Pa and μ is the dynamic viscosity in Pa s.

A mass balance of each species is given by:

$$\frac{\partial c_i}{\partial t} = -\nabla\cdot\boldsymbol{N_i} \qquad (2.3)$$

The transport of species through the electrolyte is described using the Nernst-Planck equations.

$$\boldsymbol{N}_i = -D_i\nabla c_i - z_i u_{m,i} F c_i \nabla\phi + \boldsymbol{u}c_i \qquad (2.4)$$

$$u_{m,i} = \frac{D_i}{RT} \quad (2.5)$$

Where $\mathbf{N}_i$ is the flux of the species i (H^+, Pb^{2+}, $CH_3SO_3^-$) in mol m^{-2} s^{-1}, D_i is its diffusion coefficient in m^2 s^{-1}, c_i is its concentration in mol m^{-3}, z_i is its valence, $u_{m,i}$ is its mobility in s mol kg^{-1}, ϕ is the potential of the electrolyte in V, F is Faraday's constant in C mol^{-1}, R is the gas constant in J K^{-1} mol^{-1} and T is the temperature of the electrolyte in K.

3.3 Boundary conditions

The inlet velocity of the electrolyte was prescribed as a constant parabolic velocity distribution, with the velocity set to 0 at the electrodes. The average velocity remained constant at the inlet even though the inter-electrode gap decreased with SoC (State of Charge); therefore, at a higher SoC, the volumetric flow rate was decreased. No-slip boundary conditions were applied at the electrode surface:

$$u = 0,\ v = 0 \tag{2.6}$$

At the outlet, diffusive fluxes and current are equal to zero normal to the outlet boundary. The pressure at the outlet is also set to zero (gauge)

$$-D_i \nabla c_i \cdot \boldsymbol{n} = 0, \qquad \boldsymbol{j} \cdot \boldsymbol{n} = 0, \quad p = 0 \tag{2.7}$$

The concentration of the species at the inlet were calculated using an ordinary differential equation assuming perfect mixing in the reservoir. The concentration at the outlet was volumetrically averaged with the concentration of the reservoir at the previous time step.

$$c_{in,i} = \int \frac{L}{V} \left(\int_{outlet} \boldsymbol{N}_i \cdot \boldsymbol{n}\, dS - \int_{inlet} \boldsymbol{N}_i \cdot \boldsymbol{n}\, dS \right) dt \tag{2.8}$$

Where L is the length of the electrode-electrolyte interface and V is the total electrolyte volume

The electrode-electrolyte boundary was set to move towards the opposite electrode as the volume of deposited material grew. This was calculated using Faraday's law, Eq (2.9) assuming 100% efficiency of the deposition reactions at the electrodes and the assumed density values for Pb and PbO_2 (see Table 3-2).

$$m_i = \frac{QM_i}{Fz} \tag{2.9}$$

The electrode reaction kinetics are described using the Butler-Volmer equation, described by Eq (2.10) and Eq (2.11) for the negative and positive reactions, respectively. To account for the availability of solid species in the reaction kinetics, the equation was modified so that when the solid surface concentration approached 0, the exchange current density also tended to 0.

Negative electrode:

$$i_{loc} = Fk_{0,Pb}c_{Pb^{2+}}\left(e^{\left(\frac{\alpha o,negF\eta neg}{RT}\right)} - e^{\left(\frac{-\alpha r,negF\eta neg}{RT}\right)}\right) \quad c_{Pb} > 0 \quad (2.10)$$

$$i_{loc} = 0 \qquad c_{Pb} = 0$$

Positive electrode:

$$i_{loc} = Fk_{0,PbO_2}c_{Pb^{2+}}\frac{c_{H^+}}{c_{H_0^+}}\left(e^{\left(\frac{\alpha o,posF\eta pos}{RT}\right)} - e^{\left(\frac{-\alpha r,posF\eta pos}{RT}\right)}\right) \quad c_{PbO2} > 0 \quad (2.11)$$

$$i_{loc} = 0 \qquad c_{Pb} = 0$$

Where i_{loc} is the local current density in A m^{-2}, $k_{0,Pb}$ and $k_{0,PbO2}$ are the rate constants for the negative and positive reactions respectively in m s^{-1}, α is the transfer coefficient with subscripts o and r for the anodic and cathodic reactions and pos and neg for the positive and negative reactions respectively and the subscript 0 represents an initial condition. η is the overpotential in V and is given by Eq (2.12).

$$\eta = E_{ext} - \phi - E_{eq} \qquad (2.12)$$

Where E_{ext} is the external potential and E_{eq} is the equilibrium potential at each electrode in V.

The values for E_{eq} are calculated using the Nernst equation, Eq (2.13).

Negative $$E_{Eq} = E_0 + \frac{RT}{zF}ln(c_{Pb})$$

Positive $$E_{Eq} = E_0 - \frac{RT}{zF}ln\left(\frac{c_{Pb}}{c_{H^+}}\right) \qquad (2.13)$$

Where E_0 is the standard reduction potential in V, R is the universal gas constant in J K^{-1} mol^{-1}, T is the temperature in K, Z is the valence of the reaction and c is the concentration of the species in subscript in mol m^{-3}.

The kinetics of the side reaction were described using Eq (2.14).

$$i_{loc} = F\left(k_{f,PbO}c_{PbO}^2e^{\left(\frac{F\eta pos}{RT}\right)} - c_{H^+}c_{PbO_2}k_{b,PbO}e^{\left(\frac{F\eta pos}{RT}\right)}\right) \qquad (2.14)$$

Where $k_{f,PbO}$ is the forward rate constant for the side reaction, and $k_{b,PbO}$ is the backward rate constant for the side reaction.

The potential at the negative electrode surface is set to zero:

$$\varphi = 0 \tag{2.14}$$

At the positive electrode surface, the average current density is set to the applied current.

3.3.1 Moving Mesh

Two techniques are available to mesh the system as the geometry changes: a moving mesh and an adaptive mesh. In the moving mesh technique, the number of elements remains constant. Whereas, in an adaptive mesh technique, the geometry is re-meshed at certain intervals to reduce the computational cost. In this study, a moving mesh is applied to capture the change in deposit geometry with state of charge. This is because the areas of interest are close to the electrode boundaries, which require multiple boundary layer elements. In this study, the number and size of the boundary elements remain constant. Therefore, only a marginal benefit could be gained by using an adaptive mesh. This small advantage may be lost due to the additional computational effort of re-meshing. The simpler moving mesh technique is therefore chosen.

The geometry for the model initially consists of a fluid domain representing the electrolyte and two solid domains, one at either side of the fluid domain. The left and right solid domains represent the negative electrode and the positive electrode, respectively. Initially, the solid domains are both 1 mm thick and the fluid domain, and hence the inter-electrode gap, is 12 mm thick. As the cell is charged, the sizes of the solid domains grow and the fluid domain decreases in size correspondingly. The size of the electrodes is calculated simply using Faraday's law, Eq(2.9) and typical values of density for Pb, PbO_2 and PbO, as described in Table 3-2. Eq(2.15) shows the equation used to calculate the electrode thickness.

$$d_e = d_{e,0} + \sum_i \frac{\int I_i dt \, M_i}{F z_i \rho A_e} \tag{2.15}$$

Where d_e is the thickness of the electrode, e, A_e is the electrode area and I_i is the local reaction current density for each respective species, I, averaged over the respective electrode surface, e.

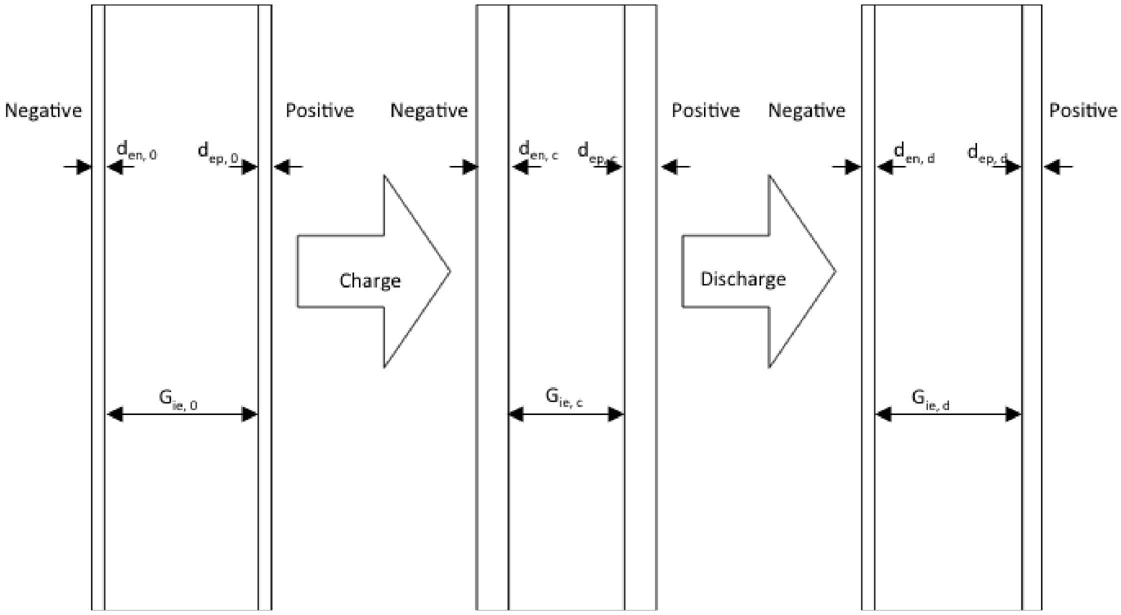

Figure 3-1: Geometry as it changes from clean electrodes (left) to electrodes with deposits combined into a single solid domain at each electrode (right). G_{ie} is the inter-electrode gap, d_{ep} and d_{en} are the positive and negative solid domain thicknesses respectively. Subscript 0 represents before cycling, c represents after charging and d after discharging.

Because the geometry is changing as the model moves, the mesh needs to adapt accordingly. Where de is the thickness of the electrode, e, Ae is the electrode area and Ii is the local reaction current density for each respective species, I, averaged over the respective electrode surface, e.

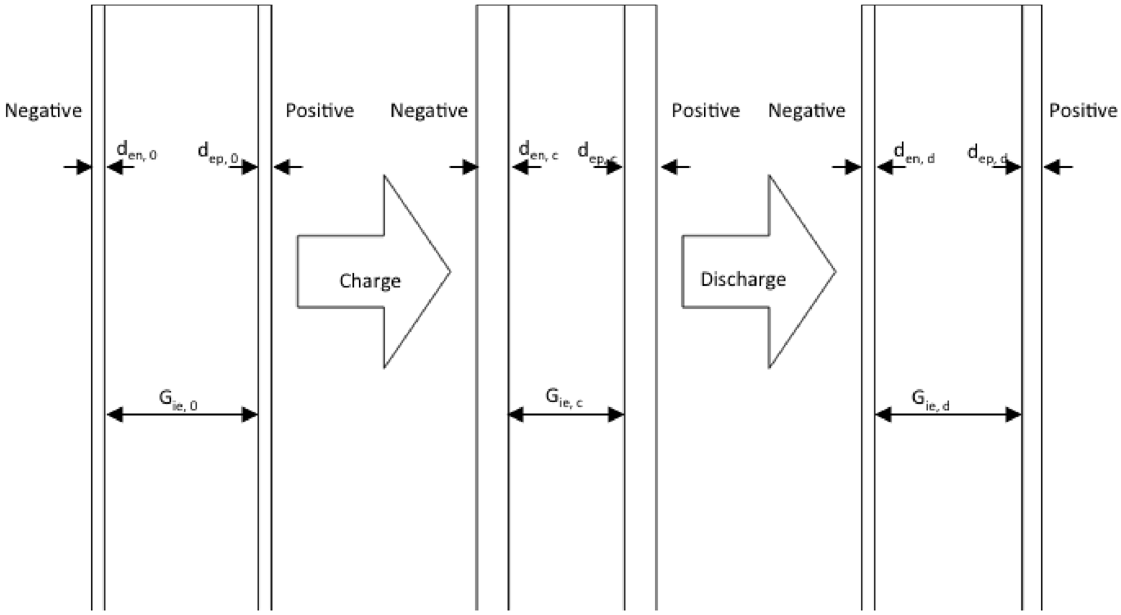

Figure 3-1 shows the change in the model geometry as the cell is charged and discharged. Initially, d_{ep} and d_{en} represent only the carbon polymer electrode material. After charging, the values for d increase and therefore the inter-electrode gap, G_{ie}, decreases. When the cell discharges, d_{en} returns to very close to $d_{en,0}$. However, due to the formation of some PbO, $d_{ep,d}$ is larger than $d_{ep,0}$.

The mesh used in this study is shown in Figure 3-2. A rectangular mesh is used with 30 elements distributed across the width of the liquid domain and 60 along the length of the cell. A further 15 boundary layer elements are added at each electrode surface on the liquid side of the electrode. In total, there are 3600 elements. The mesh sensitivity was checked using double the number of elements at the boundary and in each direction. No change to the results was found.

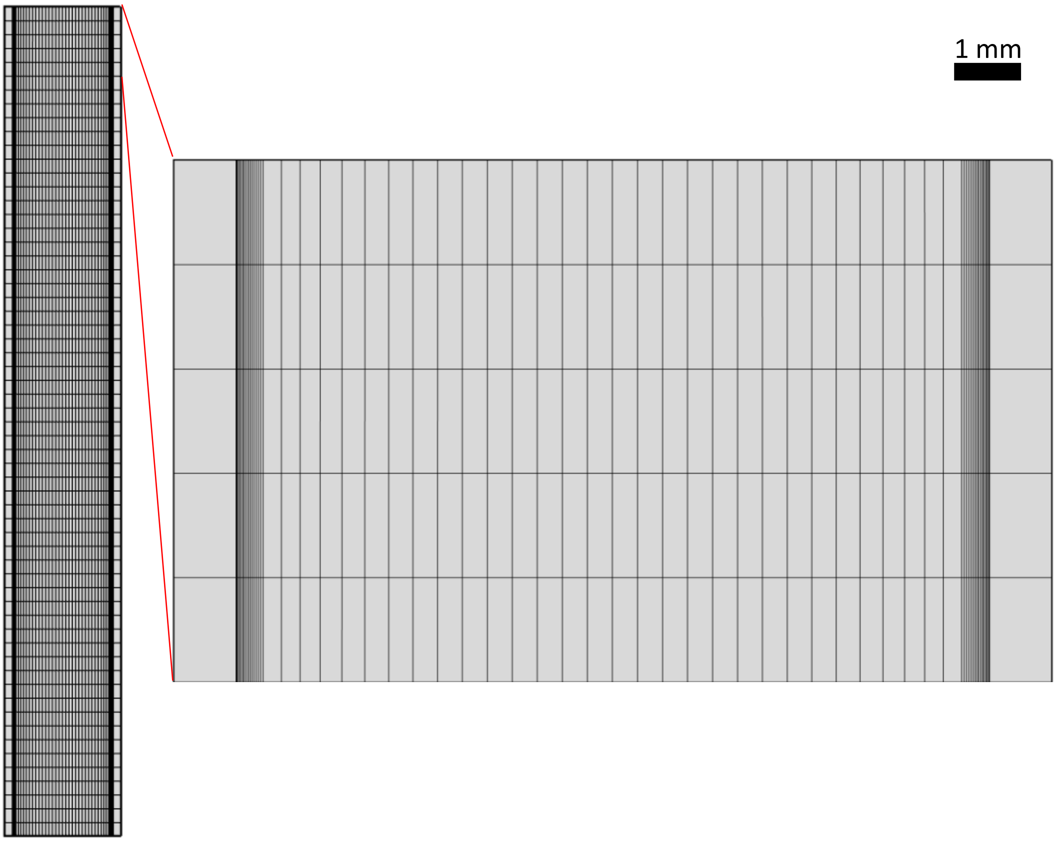

Figure 3-2: A snapshot of the mesh used for all simulations. The full mesh is shown on the left and a zoomed section is shown on the right. The mesh shown is at t = 0

3.4 Initial conditions

The initial conditions of the model are summarised in Table 3-1.

Table 3-1: Initial values for variables used in the numerical model.

Symbol	Variable	Value
u	Average inlet velocity	2.3 m s^{-1}
C_{PbII}	Pb^{2+} concentration	1000 mol dm^{-3}
C_{H+}	H^+ concentration	500 mol dm^{-3}
T	Temperature	300 K
V	Volume of electrolyte	3.6 dm^3
G_{ie}	Interelectrode gap	12 mm
d_e	Electrode thickness	1 mm

3.5 Parameters

The parameters used in the model are summarised in Table 3-2.

Table 3-2: Summary of parameters used in all simulations.

Symbol	Parameter	Value
D_{PbII}	Pb^{2+} diffusion coefficient [13]	7.0×10^{-10} m^2 s^{-1}
D_H	H^+ diffusion coefficient [13]	9.3×10^{-9} m^2 s^{-1}
$k_{0,Pb}$	Negative electrode reaction rate constant	2.1×10^{-7} m s^{-1}
$k_{0,PbO2}$	Positive electrode reaction rate constant	2.5×10^{-7} m s^{-1}
$K_{0b,PbO}$	Backward side reaction rate constant	4.5×10^{-7} mol m^{-2} s^{-1}
L	Cell length	0.1 m
M_{Pb}	Molar mass of lead [23]	207.21 g mol^{-1}
M_{PbO2}	Molar mass of lead dioxide [23]	239.2 g mol^{-1}
M_{PbO}	Molar mass of lead oxide [23]	223.2 g mol^{-1}
ρ_{Pb}	Density of Lead [24]	11.337 g cm^{-3}
ρ_{PbO2}	Density of Lead dioxide [24]	9.65 g cm^{-3}
ρ_{PbO}	Density of Lead oxide [24]	9.53 g cm^{-3}
t_{rest}	Rest time period	120 s

3.6 Numerical details

Each simulation used the same solver configuration. The time-stepping the solver used was a backward differentiation formula (BDF) method, as it is known for its stability. The order of accuracy was limited to either one or two. The BDF method uses solutions from previous time steps to approximate the derivative of an equation. A non-linear controller is used for further stability.

The solver used is a multifrontal massively parallel sparse direct solver (MUMPS) and the default COMSOL values are used. For the fluid flow, P1 + P1 discretisation (first-order elements are used for both pressure and velocity) and the solution is stabilised using streamline diffusion and crosswind diffusion methods. For the remaining equations, second-order elements are used.

4 Results and Discussion

The modelled cell was cycled for two charge-discharge cycles at constant currents of 20 mA cm^{-2} and 30 mA cm^{-2}. This is shown in

Figure 4-1: A simulated cell voltage vs time at 20 mA cm-2. Two charge-discharge cycles are simulated each with a 24 hour charge and a discharge to 1.2 V. The two-step charging mechanism is included in the second charge.

With each current density, the cell was charged to a constant Pb utilisation, so the cell charged at a higher rate was charged for a correspondingly shorter time. It can be seen that the cell charged at a higher rate also had greater overpotentials, as expected.

It can also be seen that the overpotential of the cells with the moving mesh are marginally smaller than those with no change in geometry, due to the net change in resistance over all domains. As the deposits grow, there is increasing ohmic resistance, particularly from the PbO_2, while the inter-electrode gap diminishes and the electrolyte conductivity varies as a function of SoC speciation.

During the first charge period, the voltage starts at circa 2.0 V and steadily rises to 2.1 V due to consumption of Pb^{2+} from the electrolyte and increasing electrode deposits. On discharge, the voltage decreases from 1.7 V to circa 1.55 V before a rapid decrease in voltage to 1.2 V due to a decreasing mass of electrode deposits available for the discharge reaction. On the second charge, there is initially a lower charge voltage as PbO_x is converted to PbO_2 at the positive electrode. Once the PbO_x is consumed by the reaction, the main reaction becomes dominant again and the voltage rises to a voltage comparable to that seen in the first charge. This is consistent with experimental results previously reported [21].

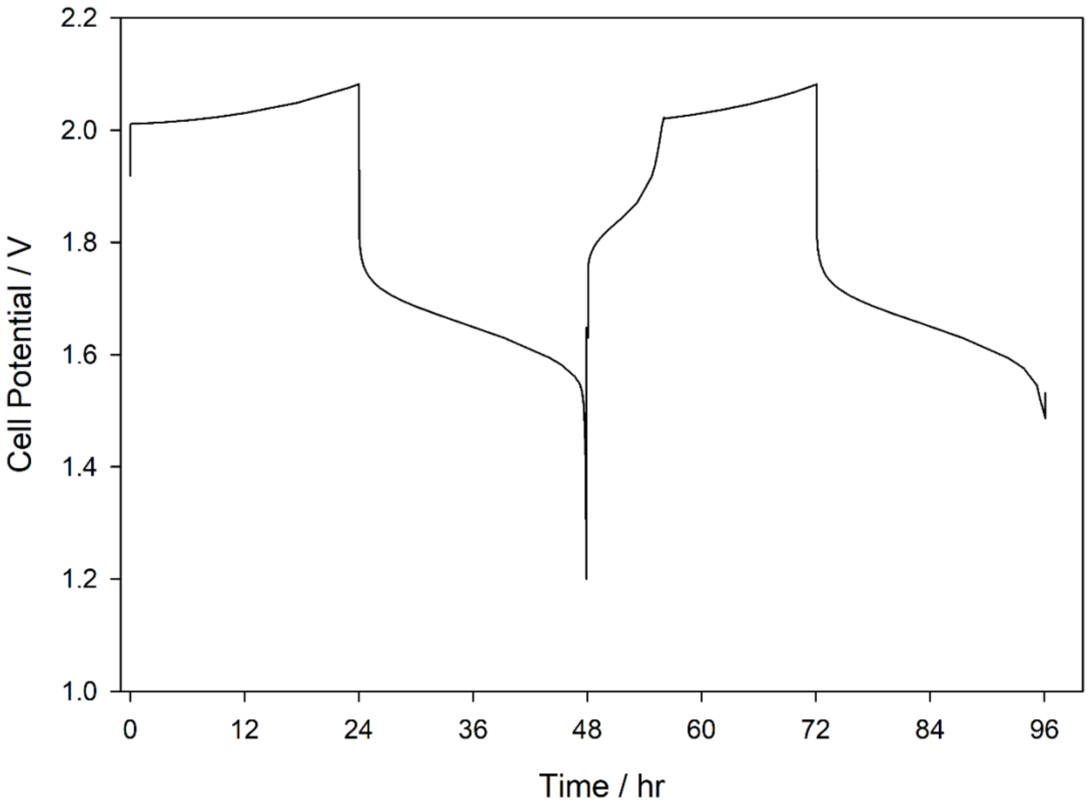

Figure 4-1: A simulated cell voltage vs time at 20 mA cm-2. Two charge-discharge cycles are simulated each with a 24 hour charge and a discharge to 1.2 V. The two-step charging mechanism is included in the second charge.

When a moving mesh is applied over the first cycle, it is seen that the overpotential is lower than when a static mesh is used, Figure 4-2. At both 20 mA cm^{-2} and 30 mA cm^{-2}, during charge, the cell potential is lower and during discharge, it is higher when a moving mesh is implemented. In both cases, as the cell is charged, this differential in cell voltage increases with time. During discharge, the difference in both cases is minor. The difference is greatest when the higher current density is applied. An overpotential which increases with time and with current density suggests this could be primarily due to a change in resistance of the cell. If only a static mesh is used, a higher potential will be predicted, which would lead to an overestimate of SoC in a real system.

As the deposits form on the electrodes, the resistance of the electrodes changes due to the change in geometry. Furthermore, as the electrolyte domain reduces in size with the formation of deposits, the concentrations of species in the electrolyte also change with SoC. Hence, the resistance of the electrolyte changes further.

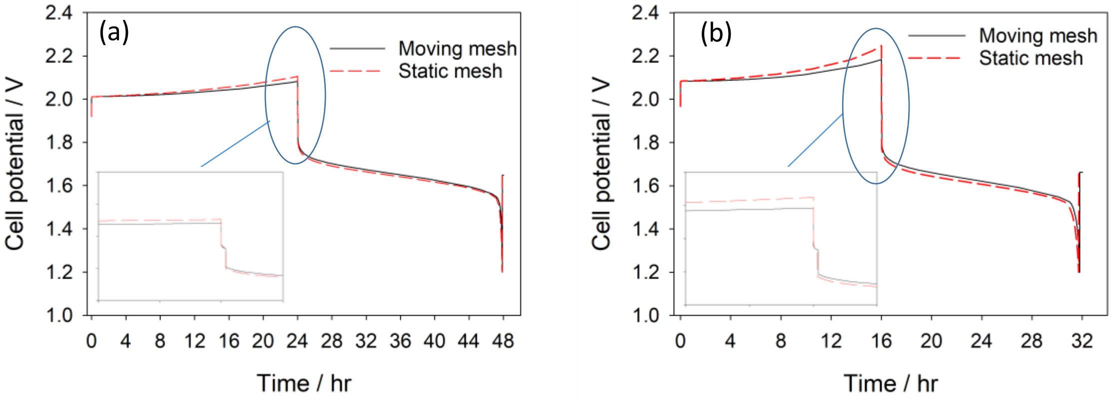

Figure 4-2: Cell voltage vs time for one cycle at 20 mA cm-2 (a) and 30 mA cm-2 (b) for static and moving meshes.

The method used to calculate the resistance of the deposits assumes uniform conductivity. In this study, it is assumed that the deposits are uniform and compact. As such, the conductivity values for bulk Pb and PbO_2 species are used. While flat two-dimensional electrode deposits are difficult to achieve in reality, this is the target for SLFB design and it is still possible to extract meaningful trends in cell resistance and flow rate using this technique. The value used for the conductivity of the lead deposit at the negative electrode is 50000 S cm^{-1} [25]. At the positive electrode, any PbO in the deposit was ignored. The deposit was therefore assumed to be entirely PbO_2. The conductivity of PbO_2 ranges from 10^3 - 10^4 S cm^{-1} for α-PbO_2 and β-PbO_2, respectively [26]. A mixture of the two forms was assumed and a value of 5000 S cm^{-1} was used for the conductivity of the positive electrode. The value used for the resistivity of the carbon polymer electrodes was 0.0006 Ω cm and was taken from the datasheet for SGL Sigracell PV15, which has been previously used in SLFB development [27].

Figure 4-3 describes the change in cell resistance, measured across the electrolyte inlet over two full cycles, each consisting of a 24 hour charge and a discharge to 1.2 V. The cell resistance is seen to change by a factor of three between clean electrodes and fully formed deposits. The majority of the cell resistance is due to the electrolyte, with just 1.6×10^{-6} Ω due to the solid phases at the maximum deposit thickness, a negligible amount compared to the ~10^{-2} Ω of the electrolyte. Due to the change in the inter-electrode gap when a moving mesh is used, there is a significant change in the resistance of the electrolyte when compared to the static mesh. The cell resistance after charging is 33% lower in the moving mesh when compared to the static mesh simulation with resistances of 0.0116 Ω and 0.0172 Ω, respectively. This difference is reduced to 9% after discharge when the moving mesh gives 0.0230 Ω and the static mesh gives 0.0250 Ω.

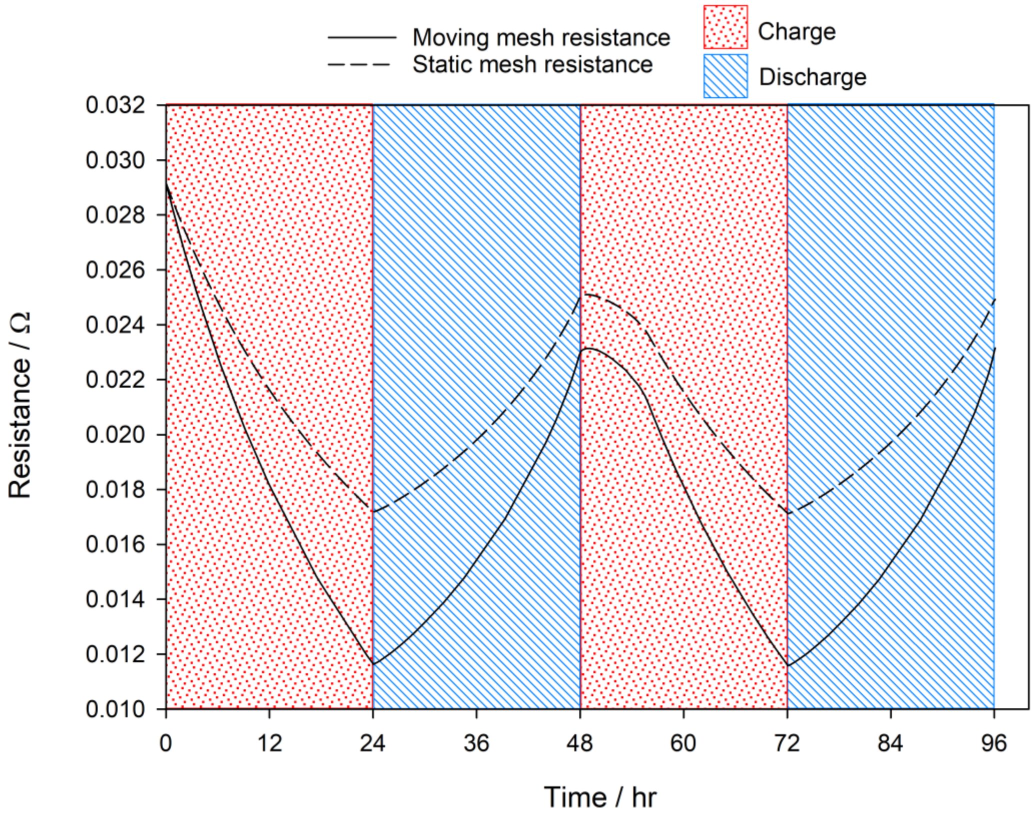

Figure 4-3: Cell and electrolyte resistance vs time for static and moving mesh simulations. The cell resistance includes the resistance of the electrolyte deposits and the carbon electrode. Both resistances are measured across the electrolyte inlet. The cell was run at 20 mA cm^{-2}.

This fluctuation in resistance is likely to be an underestimate due to neglecting the presence of an insoluble discharge product, PbO, a compound which has a much higher resistance than PbO_2, and the calculated resistance of the electrolyte which is significantly lower than the conductivity measurements by Krishna et al. would suggest [28]. The diffusion coefficient will change as a function of electrolyte composition, which would be consistent with the conductivity measurements by Krishna et al. In this simulation, the electrodes have a minimal effect on the resistance of the cell. The variation in resistance due to the deposits is 0.5 μΩ.

Figure 4-4 shows the Pb^{2+} concentration profiles of a section of the cell comparing the simulation run with a moving mesh and without the moving mesh at 20 mA cm^{-2}. Generally, a similar concentration profile is seen when comparing the two methods and the bulk concentration is almost identical in both cases. However, the change in geometry leads to a shallower gradient close to the positive electrode. With a more sophisticated understanding of mechanisms, this difference in concentration close to the electrode may be significant.

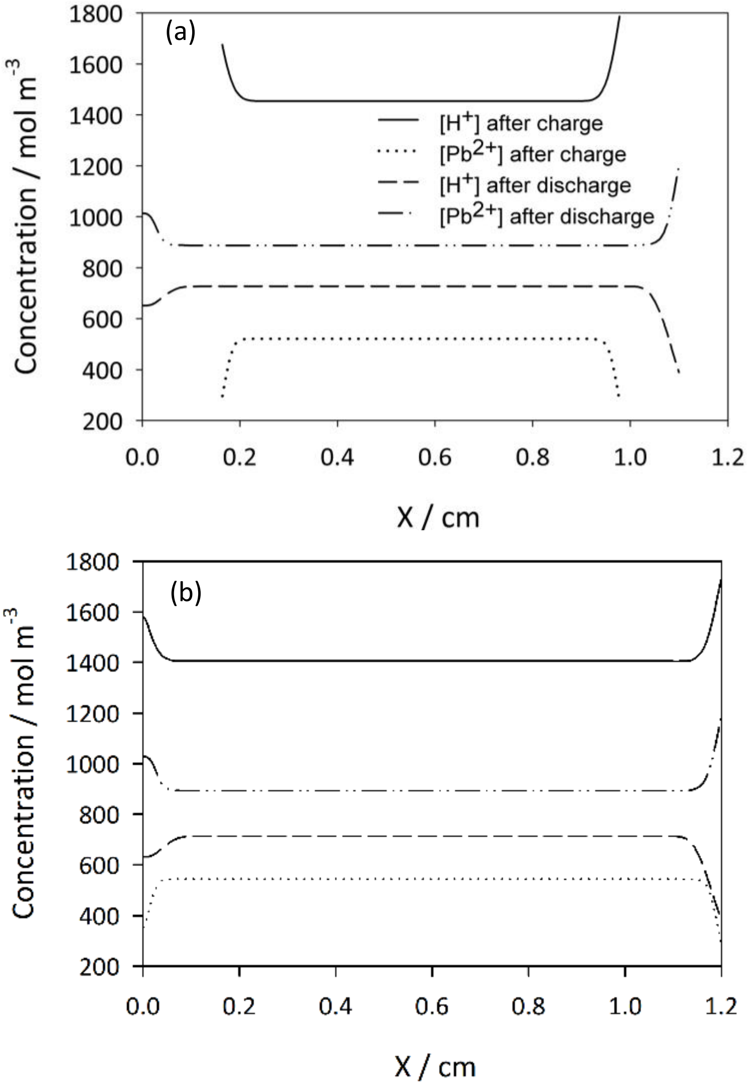

Figure 4-4: Concentration profiles of the SLFB with (a) and without (b) a simulated change in geometry. A current density of 20 mA cm^{-2} is used.

Figure 4-5 shows the volumetric flow rate of the electrolyte as the cell is cycled during the moving mesh and static mesh simulations. As expected, the static mesh shows a constant flow rate as both the geometry and the velocity were both constant. The moving mesh simulation, however, shows a significant difference in flow rate ranging from 27.8 $cm^3 s^{-1}$ to 18.6 $cm^3 s^{-1}$. In order to cycle the cell effectively, a battery management system for the flow cell would need to take this variation into account for control of the pump.

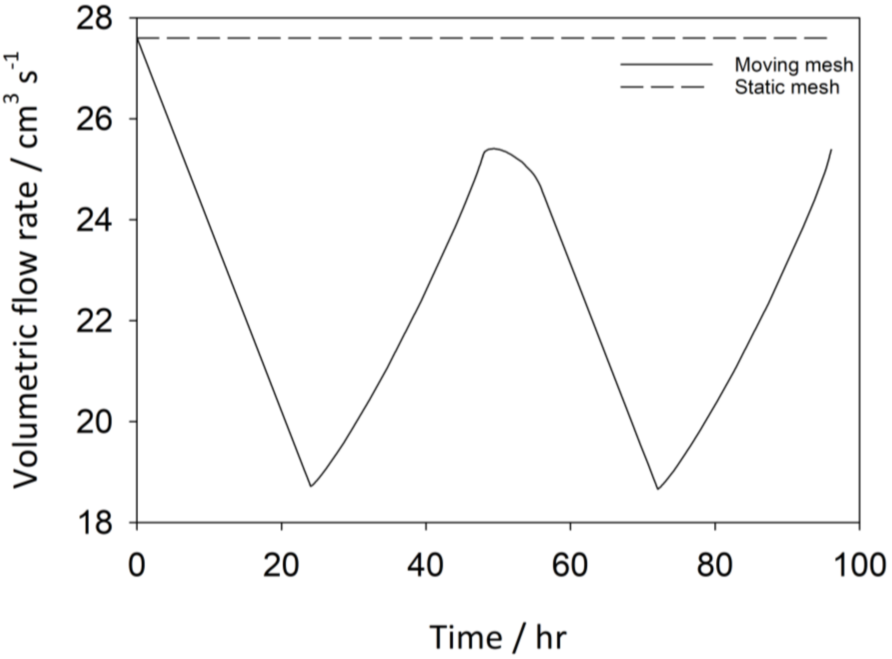

Figure 4-5: Volumetric flow rate vs time of the cell cycled at 20 mA cm-3 for both the static mesh and the moving mesh.

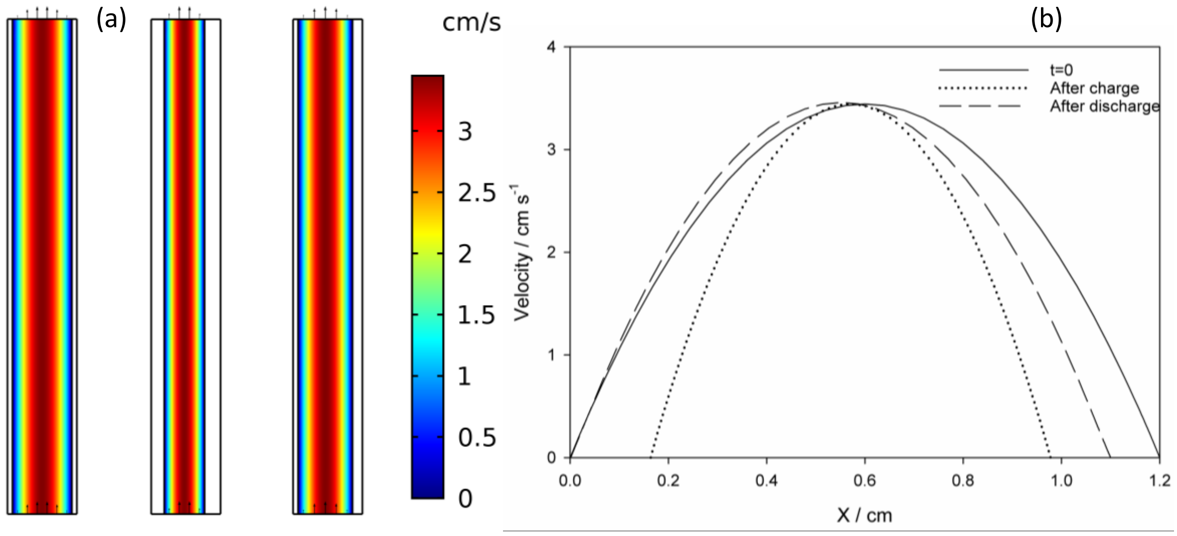

Figure 4-6: Velocity profile of the electrolyte before the first charge, after the first charge and after the first discharge (a). The distribution of the velocity across the line connecting the mid-point of both electrodes shows the parabolic shape and average velocity is maintained.

Figure 4-6 shows the electrolyte velocity profile over the liquid domain, (a), and the distribution of the y-component of velocity over a line drawn across the centre of the electrolyte domain, (b). The y-component (vertical) of the velocity dominates while flow in the x-direction (horizontal) is negligible. As explained in section 3.3, the average velocity is constant. Therefore, as shown in Figure 4-5, the volumetric flow rate varies as the liquid domain changes size with SoC. The flow remains parabolic throughout the simulation, with a maximum velocity of 3.46 cm s^{-1} at the centre of the inter-electrode gap. The velocity is zero at the boundaries, in line with the no-slip boundary condition at the electrode surfaces. A parabolic velocity profile is applied at the inlet and so the velocity profile is consistent along the length of the electrolyte domain.

4.1 Comparison with experimental results

The majority of experimental charge-discharge cycling of the SLFB has been with charges of between 1 and 2 hours. Results from literature, [12, 17, 29, 30], have been used to validate the model when run over a 1 hour charge alongside experimental data measured by the authors. The cell potentials seen during the second charge and subsequent discharge in studies where a current density of 20 mA cm^{-2} was used have been compiled and the average values are plotted against the simulated and experimental cell potential in Figure 4-7. The simulated voltage profile is 1.85 V at the beginning of the charge. It then steadily rises to circa 2.00 V by 3000 s with a maximum gradient at circa 2000 s.

The resistance between the electrode surface and the tab on the current collector, measured using a Fluke BT510 portable battery analyser, was found to be approximately 30 mΩ at each electrode. This resistance is not included simulated and hence the experimental voltage profile has been adjusted to compensate accordingly. The simulated voltage profile broadly matches the experimental curve. However, the change between the voltages of the characteristic two-step charging mechanism is less sudden in the simulated result and the cell potential during the first step occurs at circa 70 mV lower in the experimental result. The literature cell potentials are taken at the beginning and end of the charge with the point of maximum gradient used as the point of transition. The average initial and final literature potentials are 1.86 V and 2.02 V, respectively. The turning point occurs at 1620 s, a reasonable match with the simulated and experimental results from this work. However, there is also significant variability between the potentials of these two steps in the literature results. While the potential during the second step is consistent, the potential of the first step varies significantly between studies. The difference between cell potentials during these two steps ranges from 100 mV to 200 mV. These factors support the evidence that the mechanism of the two-step charging is more complex than the simple PbO side reaction included here and elsewhere. A better understanding of this area is therefore required.

There is a moderate discrepancy between the simulated and experimental cell voltage during discharge; the simulated cell voltage is approximately 1.6 compared with the experimental value of 1.55 V and the literature value of 1.48 V. The literature values are from a range of systems with different inter-electrode gaps, starting Pb and free acid concentrations and different total volumes of electrolyte. The cell potential at the end of the charge, where it is assumed only the main electrode reactions take place match closely between simulated, experimental and data from the literature. Other variables that may contribute to a change in resistance, such as the contact resistances in the cell are also not included in the model. The change in resistance due to these factors is likely responsible for the difference in cell potential seen during discharge. It should be noted that this paper aims to implement a moving mesh to take account of Pb and PbO_2 deposit formation/dissolution to simulate the SLFB system better. During both charge and discharge, the voltages derived using a moving mesh are closer to the observed experimental values than for the static mesh. On the timescale of one-hour charge/discharge periods, the difference is small (<10 mV); however, as shown in figure 3-2 over more typical operational periods for the SLFB (>1 hr), the difference can be over 100 mV. This demonstrates a significant improvement in simulation for the moving mesh approach. Over sequential charge/discharge cycling, the voltage and SoC are more accurately simulated.

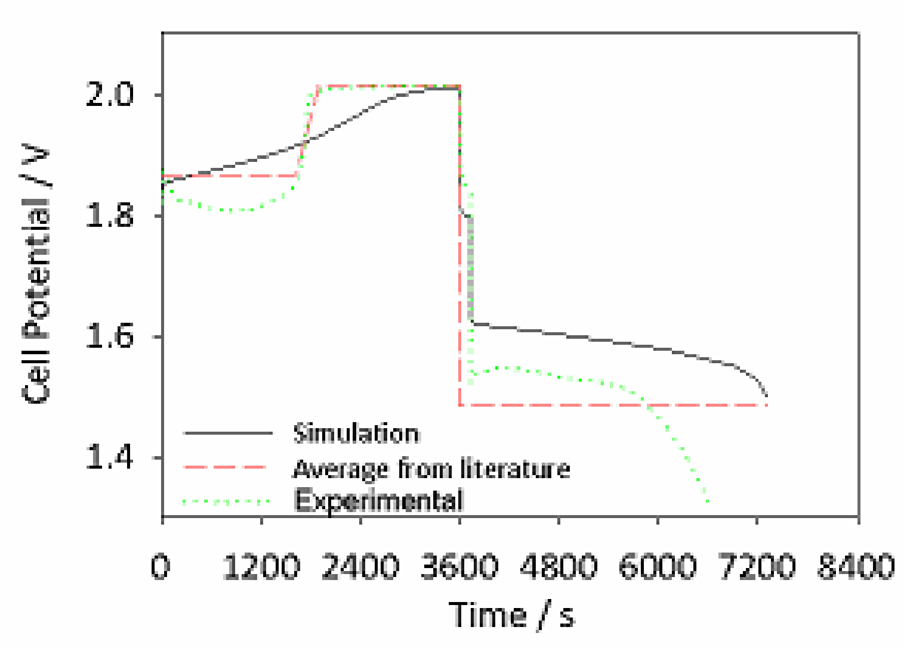

Figure 4-7: A comparison of simulated cell potential during the second charge with average values seen in the literature and experimental for the second charge-discharge cycle at a constant current density of 20 mA cm^{-2}.

5 Conclusions

A two-dimensional time-dependent numerical model has been produced to simulate the operation of the SLFB. A moving mesh technique has been deployed to simulate the deposition of solid Pb and PbO_2 at the negative and positive electrodes respectively and accounts for the change in geometry that results from these deposits. The change in geometry results in a greater resistance of the solid domains due to an increase in thickness but, more significantly, accounts for the overall decrease in electrolyte resistance as the cell increases in SoC. The change in geometry also allows for a higher value for the concentration of acid species locally to the electrodes after charging. The significance of implementing this moving mesh model is the ability to model flow battery systems involving a solid/liquid phase change and hence the varying reaction chamber geometry as a function of state of charge. This has direct implications for other systems such as the Zn-Br, Zn-air, Zn-Ce, etc. With proof of concept of this modelling approach demonstrated in this paper, future work can be carried out to refine the electrochemical and thermodynamic problems.

Acknowledgements

The authors would like to acknowledge the financial support received from the Engineering and Physical Sciences Research Council (EPSRC) through the Centre for Doctoral Training in Energy Storage and its Applications grant EP/L016818/1.

List of Symbols

c	Concentration
D	Diffusion coefficient
d	Domain thickness
E	Potential
e	electrode
e^-	Electron
F	Faraday’s constant
G	Inter-electrode gap
H^+	Proton
H_2O	Water
i	species
j	Current density
k	Rate constant
L	Length of electrode
m	Mass
M	Mass number
N	Flux of species
n	Normal vector
p	pressure
Pb	Lead
Pb^{2+}	Lead (II) ions
PbO	Lead oxide
PbO_2	Lead dioxide
Q	Charge
R	Gas constant
t	Time
T	temperature
U	Electrolyte velocity

V	Electrolyte volume
v	Velocity
z	Valence
α	Transfer coefficient
η	Overpotential
μ	Dynamic viscosity
ρ	density
ϕ	Ionic potential

References

[1] B. Dunn, H. Kamath and J.-M. Tarascon (2011) Electrical energy storage for the grid: a battery of choices, *Science,* **334** (6058), pp. 928-935, 10.1126/science.1212741

[2] M. Krishna, E.J. Fraser, R.G.A. Wills and F.C. Walsh (2018) Developments in soluble lead flow batteries and remaining challenges: An illustrated review, *Journal of Energy Storage,* **15**, pp. 69-90, 10.1016/j.est.2017.10.020

[3] P. Leung, X. Li, C. Ponce de Leon, L. Berlouis, C.T.J. Low and F.C. Walsh (2012) Progress in redox flow batteries, remaining challenges and their applications in energy storage, *RSC Advances,* **2** (27), pp. 10125-10156, 10.1039/c2ra21342g

[4] G.L. Soloveichik (2015) Flow batteries: current status and trends, *Chemical reviews,* **115** (20), pp. 11533-11558, 10.1021/cr500720t

[5] A.Z. Weber, M.M. Mench, J.P. Meyers, P.N. Ross, J.T. Gostick and Q. Liu (2011) Redox flow batteries: a review, *Journal of Applied Electrochemistry,* **41** (10), pp. 1137-1164, 10.1007/s10800-011-0348-2

[6] P. Leung, A. Shah, L. Sanz, C. Flox, J. Morante, Q. Xu*, et al.* (2017) Recent developments in organic redox flow batteries: a critical review, *Journal of Power Sources,* **360**, pp. 243-283, 10.1016/j.jpowsour.2017.05.057

[7] R. Ye, D. Henkensmeier, S.J. Yoon, Z. Huang, D.K. Kim, Z. Chang*, et al.* (2018) Redox flow batteries for energy storage: a technology review, *Journal of Electrochemical Energy Conversion and Storage,* **15** (1), p. 010801, 10.1115/1.4037248

[8] US Department of Energy (2019), DOE Global Energy Storage Database. Available: https://energystorageexchange.org/ [Accessed:10/01/2019].

[9] M.D. Gernon, M. Wu, T. Buszta and P. Janney (1999) Environmental benefits of methanesulfonic acid: Comparative properties and advantages, *Green Chemistry,* **1** (3), pp. 127-140, 10.1039/a900157c

[10] Y. Tian, A. Bera, M. Benidris and J. Mitra (2018) Stacked revenue and technical benefits of a grid-connected energy storage system, *IEEE Transactions on Industry Applications,* **54** (4), pp. 3034-3043,

[11] S.M. Schoenung (2001) Characteristics and technologies for long-vs. short-term energy storage, *United States Department of Energy,*

[12] A.A. Shah, X. Li, R.G. Wills and F.C. Walsh (2010) A mathematical model for the soluble lead-acid flow battery, *Journal of The Electrochemical Society,* **157** (5), pp. A589-A599, 10.1149/1.3328520

[13] A. Bates, S. Mukerjee, S.C. Lee, D.-H. Lee and S. Park (2014) An analytical study of a lead-acid flow battery as an energy storage system, *Journal of Power Sources,* **249**, pp. 207-218, 10.1016/j.jpowsour.2013.10.090

[14] A. Oury, A. Kirchev and Y. Bultel (2014) A numerical model for a soluble lead-acid flow battery comprising a three-dimensional honeycomb-shaped positive electrode, *Journal of Power Sources,* **246**, pp. 703-718, 10.1016/j.jpowsour.2013.07.101

[15] M. Nandanwar and S. Kumar (2016) Charge coup de fouet phenomenon in soluble lead redox flow battery, *Chemical Engineering Science,* **154**, pp. 61-71, 10.1016/j.ces.2016.07.001

[16] M. Nandanwar and S. Kumar (2019) A modelling and simulation study of soluble lead redox flow battery: Effect of presence of free convection on the battery characteristics, *Journal of Power Sources,* **412**, pp. 536-544, 10.1016/j.jpowsour.2018.11.070

[17] M.N. Nandanwar and S. Kumar (2014) Modelling of Effect of Non-Uniform Current Density on the Performance of Soluble Lead Redox Flow Batteries, *Journal of The Electrochemical Society,* **161** (10), pp. A1602-A1610, 10.1149/2.0281410jes

[18] P. Alotto, M. Guarnieri and F. Moro (2014) Redox flow batteries for the storage of renewable energy: A review, *Renewable and sustainable energy reviews,* **29**, pp. 325-335, 10.1016/j.rser.2013.08.001

[19] J. Collins, J. Bateman and D. Pletcher, "Emerging Energy Technologies: Redox flow cells for intelligent grid management, TP No: TP/4/EET/6/I/22296," Department of Trade and Industry (DTI), 2009.

[20] D. Pletcher, H. Zhou, G. Kear, C.T.J. Low, F.C. Walsh and R.G.A. Wills (2008) A novel flow battery: A lead-acid battery based on an electrolyte with soluble lead(II) Part V. Studies of the lead negative electrode, *Journal of Power Sources,* **180** (1), pp. 621-629, 10.1016/j.jpowsour.2008.02.024

[21] D. Pletcher and R. Wills (2005) A novel flow battery: A lead acid battery based on an electrolyte with soluble lead(II) Part III. The influence of conditions on battery performance, *Journal of Power Sources,* **149** (0), pp. 96-102, http://dx.doi.org/10.1016/j.jpowsour.2005.01.048

[22] F.M. White, *Fluid Mechanics*: McGraw Hill, 2011.

[23] G.W.C. Kaye, T.H. Laby and N.P. Laboratory, *Kaye & Laby Tables of Physical & Chemical Constants*: National Physical Laboratory, 1995.

[24] R.H.P.D.W. Green, R.H. Perry, D.W. Green and Knovel, *Perry's Chemical Engineers' Handbook, Eighth Edition*: McGraw-Hill Education, 2008.

[25] R.C. Weast, M.J. Astle and W.H. Beyer, *CRC handbook of chemistry and physics* vol. 69: CRC press Boca Raton, FL, 1988.

[26] X. Li, D. Pletcher and F.C. Walsh (2011) Electrodeposited lead dioxide coatings, *Chemical Society Reviews,* **40** (7), pp. 3879-3894, 10.1039/c0cs00213e

[27] SGL (2019), SIGRACELL Bipolar Plate datasheet. Available: https://www.sglcarbon.com/en/markets-solutions/material/sigracell-bipolar-plates-and-end-plates/ [Accessed:17/03/2019].

[28] M. Krishna, L. Wallis, R. Wills, D. Hall and A. Shah (2017) Measurement of key electrolyte properties for improved performance of the soluble lead flow battery, *International Journal of Hydrogen Energy,* **42** (29), pp. 18491-18498, 10.1016/j.ijhydene.2017.05.004

[29] J. Collins, G. Kear, X. Li, C.T.J. Low, D. Pletcher, R. Tangirala*, et al.* (2010) A novel flow battery: A lead acid battery based on an electrolyte with soluble lead(II) Part VIII. The cycling of a 10 cm × 10 cm flow cell, *Journal of Power Sources,* **195** (6), pp. 1731-1738, http://dx.doi.org/10.1016/j.jpowsour.2009.09.044

[30] D. Pletcher and R. Wills (2004) A novel flow battery: A lead acid battery based on an electrolyte with soluble lead (II) Part II. Flow cell studies, *Physical Chemistry Chemical Physics,* **6** (8), pp. 1779-1785,